Research Article

Chemical Review and Letters
journal homepage: www.chemrevlett.com
ISSN (online): 2645-4947 (print) 2676-7279

The influence of pH and temperature on the alterations in the structural, optical, electronic, and photocatalytic behavior of TiO_2 powder with simultaneous addition of Fe^{2+} and Fe^{3+}

Candra Purnawan[1,2], Endang Tri Wahyuni[1,*], Indriana Kartini[1], Suherman[1]

[1]*Department of Chemistry, Faculty of Mathematics and Natural Sciences, Gadjah Mada University, Sleman, Yogyakarta, Indonesia.*
[2]*Department of Chemistry, Faculty of Mathematics and Natural Sciences, Sebelas Maret University, Surakarta, Central Java, Indonesia.*

ARTICLE INFO

Article history:
Received 24 November 2025
Received in revised form 27 January 2026
Accepted 28 January 2026

Keywords:
TiO_2 powder
Fe^{2+} and Fe^{3+}
pH
Temperature
Structural
Optical
Electronic
Magnetic
Photocatalytic

ABSTRACT

The simultaneous incorporation of Fe^{2+} and Fe^{3+} ions using co-precipitation methods with variation in pH and temperature has modified the structural, optical, electronic, magnetic, and photocatalytic activity of TiO_2 powder. The characterization of photocatalyst composites had been carried out using spectrophotometry Raman, XRD, SAA, DRS, XPS, and VSM. The higher the pH of the synthesis has caused a decrease in magnetic properties, TiO_2 crystal composition, crystal size, and band gap, but increase surface area. Meanwhile, the higher temperature synthesis (110 °C) has caused a decrease in magnetic properties, TiO_2 crystal composition, surface area, but increase crystal size, crystallinity, and band gap. Photocatalyst composites synthesized with higher pH and lower reaction temperature have shown greater photocatalytic activity.

1. Introduction

Titanium dioxide (TiO_2) is one of the photocatalysts that is widely used but has bad photocatalysis activity under visible light radiation and poor separability properties. One of the modifications of TiO_2 that has been widely developed is the addition of iron elements. Iron is a common transition metal that can reduce bandgap and provide magnetic properties. Ferric ion (Fe^{3+}) can function as dopants because both Fe^{3+} (0,64 Å) and Ti^{4+} (0,68 Å) ions have similar sizes [1-5]. And in its oxide form, it can be functioned as a photocatalyst, magnetizing agent, and adsorbents. However, so far, the doping and magnetization processes are still carried out separately and in stages with several steps.

Furthermore, one of the commonly used methods for doping or magnetizing TiO_2 is the sol-gel method using TiO_2 precursor. The process of doping TiO_2 with Fe^{3+} ions (TiO_2-Fe) using TiO_2 precursors via the sol-gel method has been performed by previous researchers and showed enhanced photocatalytic activity under visible light, but it cannot provide magnetic properties [6-9]. Separately, magnetization of TiO_2 with Iron oxide (TiO_2/Fe_xO_y) using the sol-gel method has been carried out in two stages by previous researchers and has shown magnetic properties so that it is easy to separate from the solution [10-15].

However, using TiO_2 precursors with sol-gel method for TiO_2 modification is a time-consuming, difficult reaction control, requires many chemicals, and high cost, so that it is not applicable and inefficient in the industrial waste treatment. Furthermore, the simultaneous addition of Fe^{2+} and Fe^{3+} ions to the TiO_2 precursor for doping and magnetization is quite difficult. This is because adding too many iron ions in a basic environment prevents TiO_2 crystals, whereas magnetic iron oxide cannot be formed in an acidic environment. Recent studies have also employed TiO_2 powder via hydrothermal or co-precipitation methods to simplify synthesis. However, it will be difficult because anatase TiO_2 powder is a crystal with excellent chemical and physical stability [16].

Shymanovska et al. (2021) [17] have conducted Fe^{3+}

* Corresponding author E-mail: endang_triw@ugm.ac.id
https://doi.org/10.22034/crl.2026.561838.1739

ion doping on TiO_2 Anatase and Rutile powders. The results have demonstrated that the adsorption of Fe^{3+} ions on the surface of Anatase is twice as efficacious as that of Rutile. The adsorption of Fe^{3+} ions on the TiO_2 surface causes changes in the crystal lattice, bandgap, and acidity. However, the photocatalytic activity of Safranin T degradation using Fe^{3+} doped TiO_2 is lower than TiO_2 without doping. Meanwhile, Afonso et al. (2023) [18] found that Fe^{3+}-doped TiO_2 photocatalysts lacked magnetic characteristics and had worse RhB photodegradation efficiency (<70%) than undoped TiO_2 (74%) under visible light irradiation. So, further research is needed to simultaneously enhance photocatalytic activity under visible light and improve catalyst separability through magnetization.

According to the information above, this study will modify TiO_2 powder by making TiO_2 -Fe/Fe_2O_3 composites through research on the influence of important factors such as composition, pH, and synthetic temperature. On the previous research, alterations in the molar ratio of Fe^{2+}:Fe^{3+} and Fe_2O_3 to TiO_2 play a crucial role in modifying the properties and activity of TiO_2 powder. In addition to this composition, the pH and temperature of the synthesis can affect the photocatalyst's properties and activity. Changes in pH and reaction temperature will provide differences in the reaction mechanism for the formation of iron oxide and the interaction between iron oxide and TiO_2. The influence of Fe^{2+} and Fe^{3+} addition under varying pH and temperature on iron oxide formation, bonding and functional groups, crystallinity, crystal size and composition, band gap, electron binding energy, surface area, and magnetic properties of synthesized photocatalysts is of particular interest. Modifications to these properties will influence the separability and photocatalytic activity under visible light irradiation, such as photoreduction of Chromium hexavalent (Cr (VI)) and photodegradation of MV. To determine the effects, the photocatalyst composite will be characterized using FTIR, Raman, XRD, SAA, TEM, DRS, XPS, and VSM.

2. Materials and Methods

2.1. Materials

Titanium(IV) Oxide Anatase >99% (TiO_2, Sigma-Aldrich), Iron(III) Chloride hexahydrate ($FeCl_3.6H_2O$, Merck), Iron(II) Chloride Tetrahydrate ($FeCl_2.4H_2O$, Merck), Sodium Hydroxide (NaOH, Merck), Isopropanol (C_3H_8O, Merck), Potassium dichromate ($K_2Cr_2O_7$, Merck), Methyl violet (C. I. 42535, $C_{24}H_{27}N_3.ClH$, Loba Chemie PVT, LTD), Demineralized Aqua (H_2O TDS<1.3 µS/cm, Brataco), Acetone (Merck), Nitric Acid (HNO_3, Merck), Diphenylcarbazide ($C_{13}H_{14}N_{4O}$, Merck), Chloroform ($CHCl_3$, Merck), Phosphoric Acid 85% (H_3PO_4, Merck).

2.2. Instruments

A set of glassware (Pyrex), magnetic stirrer (Cimarec, Thermo Scientific), Oven (Memmert), Muffle Furnace (JKI JK-SX2-5-12N), Shaker (Kang Jian, KJ-210BD), Analytical balance (Sartorius A6 Gottingen), Universal pH paper (Merck), pH meter (OHAUS starter 300), Lux Meter (WalkLab), Reactor box and Visible lamp (Tungsten 300 Watt, Toki), UV-Vis Spectrophotometer (Shimadzu UV-1800), UV-Vis Reflectance Spectrophotometer (Shimadzu UV-2401-PC), Fourier Transform InfraRed (FTIR, Shimadzu IR Prestige-21), X-ray Diffraction (XRD, Bruker D8 Advance), Vibrating Sample Magnetometer (VSM, Quantum Design PPMS® VersaLab™ Cryogen-free 3 Tesla), Surface Area Analyzer (SAA, Quantachrome Novatouch LX-4), Scanning Electron Microscope-Energy Dispersive X-ray (SEM-EDX, Jeol Benchtop JCM 7000), Transmission Electron Microscopy (TEM, Jeol JEM-1400), X-Ray Photoelectron Spectroscope (XPS, JPS-9030 JEOL).

2.3. Procedures

2.3.1. Synthesis of TiO_2-Fe/Fe_2O_3

Composite TiO_2-Fe/Fe_2O_3 had been synthesized using TiO_2 Anatase powder, $FeCl_3.6H_2O$ and $FeCl_2.4H_2O$. A quantity $FeCl_3.6H_2O$ and $FeCl_2.4H_2O$ with constant theoretical mole ratio of Fe^{2+}:Fe^{3+} = 1:2 and TiO_2:Fe_2O_3 = 1: $\frac{1}{5}$ ($TF_{0.2}$) (mole/mole) were dissolved in 25 mL of distilled water and added with a number of TiO_2 Anatase powder in 25 mL of isopropanol. Then, 50 ml of distilled water was added to the mixture and stirred for 1 hour (400 rpm). Next, add drop by drop NaOH 10 M until the pH = 10, 12, and 14 while stirring continuously for 1 hour (700 rpm). Then the mixture was heated at 90 °C (<boiling point of water) and 110 °C (>boiling point of water) for 1 hour while stirring continuously. The black or dark gray composite formed was dried overnight at 60 °C (24 hours). After grinding into powder, the granules were calcined in a muffle furnace at 400 °C for 2 hours. The synthesized composite was rinsed with demineralized water until it reached a neutral pH and dried again overnight in a 60 °C oven (12 hours) and then characterized using Fourier Transform InfraRed (FTIR) Spectroscopy, Raman Spectroscopy, Diffused Reflectance Spectroscopy, X-Ray Diffraction (XRD) Spectroscopy, Vibrating Sample Magnetometer (VSM), Scanning Electron Microscope (SEM), Transmission Electron Microscope (TEM), Surface Area Analyzer (SAA), and X-ray photoelectron spectroscopy (XPS).

2.3.2. Photocatalytic activity of TiO_2-Fe/Fe_2O_3.

The synthesized composite was then used for photocatalytic activity testing. The photocatalytic activity test of TiO_2-Fe/Fe_2O_3 was applied for the photoreduction of Cr (VI) and photodegradation of MV. Photoreduction

of Cr (VI) and photodegradation of MV was carried out by adding 0.1 g of catalyst into 50 mL of 50 ppm substrate (Cr^{6+} or MV) solution. The solution was left for 15 minutes to provide interaction between the catalyst and substrate, then irradiated with a 300watt Tungsten lamp in a reactor box with a distance of 20 cm (7000-7250 lux) for 1 hour. After that, the catalyst was separated from the solution using an external magnetic bar. Measurement of absorbance of the solution using UV-Vis spectrophotometer at λ = 577 nm for MV and 542 nm for complex Cr (VI)-difenil carbazide solution. As a control, a photocatalysis test was conducted using TiO_2 with 300watt Tungsten lamp irradiation. The percentage of photodegradation is calculated based on the equation below.

$$E = \frac{C_0 - C_f}{C_0} \times 100\% \quad (1)$$

Where, E (%) is the photoreduction or photodegradation efficiency, C_0 and C_f are the initial and final concentration of substrate, respectively.

3. Results and Discussion

3.1. Characterization

The study will investigate the effect of temperature and pH reaction on the vibrational energy shift and functional groups, chemical bonds and electron density, formation of iron oxide, magnetic strength, crystal properties, surface area, morphology, bandgap of the composite, and its photocatalysis activity on photoreduction of Cr (VI) and photodegradation of MV dye. The modification of TiO_2 powder hopefully can improve the properties including magnetic properties and increase the photocatalytic activity in the visible light simultaneously.

3.1.1. Influence of pH synthesis

In this section, TiO_2-Fe/Fe_2O_3 photocatalyst have been synthesized with a constant mole ratio of Fe^{2+}:Fe^{3+} = 1:2 (mole/mole), TiO_2:Fe_2O_3 = 1:1/5 ($TF_{0.2}$). Meanwhile, the variation of temperature was carried out at pH = 10, 12, and 14. Based on the research, mole ratio has been affected properties and photocatalytic activities of the photocatalyst.

Raman Analysis. The pH synthesis influenced Raman inelastic scattering, as shown in Figure 1.

Figure 1 showed that calcination induces the transformation of Fe_3O_4 (blue spectra) to Fe_2O_3 (red spectra), as indicated by the disappearance of Magnetite peaks at 108.88 and 647.06 cm^{-1} and the emergence of a new peak at 241.25 cm^{-1} [19]. The shifts at 217.60 and 281.92 cm^{-1} confirm the oxidation of Fe^{2+} to Fe^{3+} during the process [20]. The increased intensity ratio of the 281.92 cm^{-1} peak to the 217.60 cm^{-1} peak further supports the increasing of Fe^{3+} after calcination.

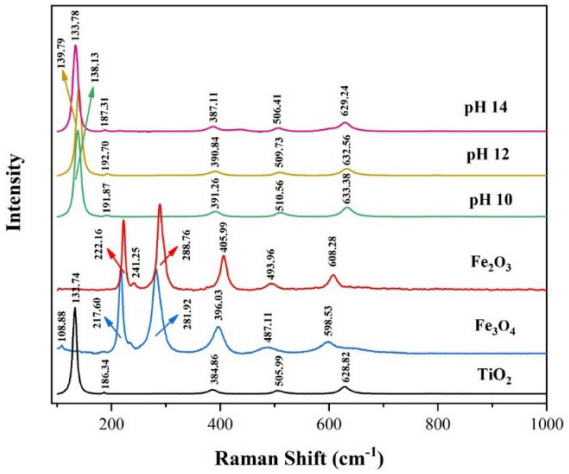

Fig. 1. Raman spectra of composites with variations in pH synthesis.

Figure 1 also indicated that as pH increased from pH = 10 to 12, peak shifts towards higher wavenumbers (blue shift) occurred, particularly the primary peak (E1g) from 138.12 cm^{-1} to 139.79 cm^{-1}. The blue shift and broadening at higher dopant levels confirm lattice deformation and defect formation due to Fe^{3+} substitution for Ti^{4+} in the TiO_2 lattice. Increasing the amount of Fe^{3+} dopant causes a shift towards higher wavenumbers (blue shift) [21-24]. The blue shift (hypochromic) indicated that the higher pH, the greater the polarization of the electron and the distortion of the TiO_2 crystal, resulting in a larger Raman shift and decreased crystallinity. The Raman peak shift can be attributed to the lattice distortion caused by the replacement of Ti^{4+} with Fe^{3+} in the TiO_2 framework. Furthermore, at pH = 12 to 14, there was a peak shift from 139.79 cm^{-1} to 133.78 cm^{-1}. Red shift (bathochromic) has shown an increase in interfacial and heterojunction interactions with increasing pH. This is due to the increase in Fe^{2+} and Fe^{3+} precipitation on the surface of TiO_2 powder as the pH increases from 12 to 14.

XRD Analysis. The pH synthesis has affected the diffractogram pattern and crystallite composition of composite using the Reitveld Refinement program HighScore Plus as shown in Figure 2. Figure 2a has shown the difference in the composition of iron oxide formed at pH 10 – 14. At pH 10, the formation of Maghemite (γ-Fe_2O_3) was more dominant than Hematite (α-Fe_2O_3). While at pH 14, the formation of Hematite (α-Fe_2O_3) was more dominant as seen from the highest intensity at 2θ = 33.14° (104) as the main peak of Hematite (α-Fe_2O_3). This was supported by refinement analysis using HighScore Plus as seen in Figure 2b.

Figure 2b showed that increasing pH had decreased the proportion of TiO_2 and maghemite while promoting hematite formation. This indicated that both TiO_2 crystallinity and maghemite formation decline, whereas hematite formation increased with higher synthesis pH. Under more alkaline conditions (pH 12–14), Fe^{2+} and Fe^{3+} ions react rapidly with hydroxyl groups (–OH),

promoting the precipitation of $Fe(OH)_2$ and $Fe(OH)_3$ [25]. At high pH (14), excess –OH weakens $Fe(OH)_2$ and $Fe(OH)_3$ interactions during the nucleation of magnetite (Fe_3O_4) and maghemite, leading to reduced maghemite formation. Further dehydration of $Fe(OH)_3$ during heating (150–450 °C) promotes the transformation into iron oxide phases [26]. Consequently, calcination predominantly converts $Fe(OH)_3$ into hematite, resulting in higher hematite content at elevated pH.

Variations in synthesis pH also influence the crystallinity and crystal size of the resulting photocatalyst composites, as shown in Figure 3. Figure 3 showed a decrease in composite crystallinity from pH 10 to 12. As observed in Figure 2, the reduction is primarily attributed to the decreased crystallinity of TiO_2 and maghemite (γ-Fe_2O_3). Under more alkaline conditions, the higher –OH concentration induces greater lattice distortion and deformation in TiO_2, leading to reduced crystallinity and smaller crystal size of both TiO_2 and the overall photocatalyst composite. However, as the pH increases from 12 to 14, the composite crystallinity rises again, mainly due to the enhanced formation and crystallinity of hematite (α-Fe_2O_3). This improvement results from the increased precipitation of $Fe(OH)_3$ at higher pH, which subsequently transforms into hematite during heating and calcination.

As shown in Figure 3, increasing the reaction pH decreases the photocatalyst crystal size. Higher alkalinity enhances –OH concentration, leading to greater lattice distortion and deformation of TiO_2, which reduces the crystal size of anatase and the overall composite. The presence of TiO_2 powder also restricts $Fe(OH)_2$–$Fe(OH)_3$ interaction during nucleation, resulting in smaller magnetite and maghemite crystals. Under high Fe^{3+} content and strongly basic conditions, particle agglomeration becomes more significant [25,27,28], hindering crystal growth and further reducing iron oxide crystal size.

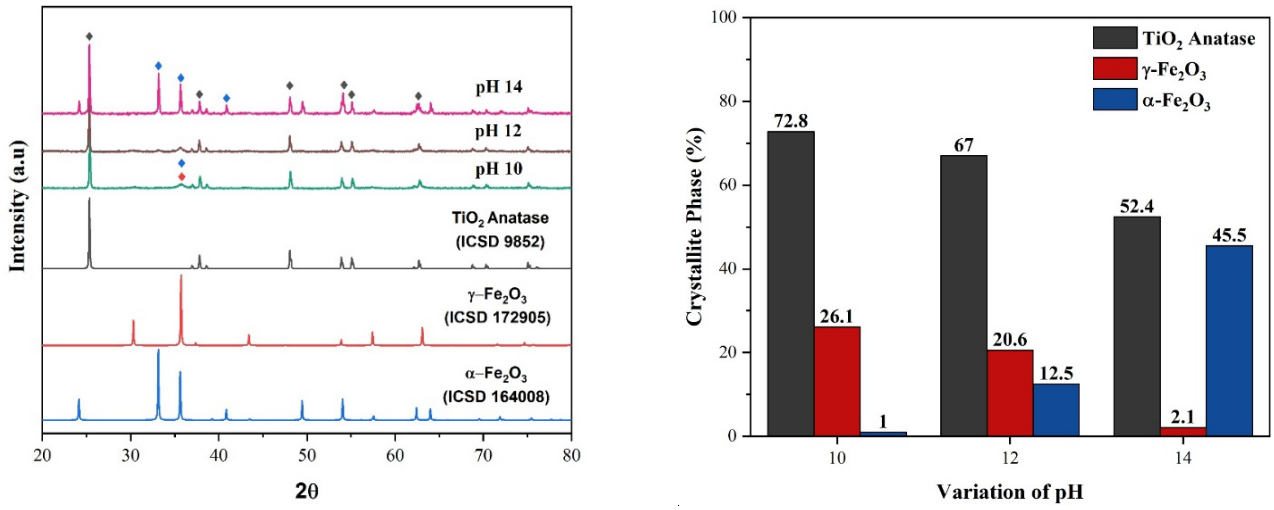

(a) (b)

Fig. 2. (a) XRD diffractogram, and (b) crystallite composition (%) of photocatalyst composite with pH variation

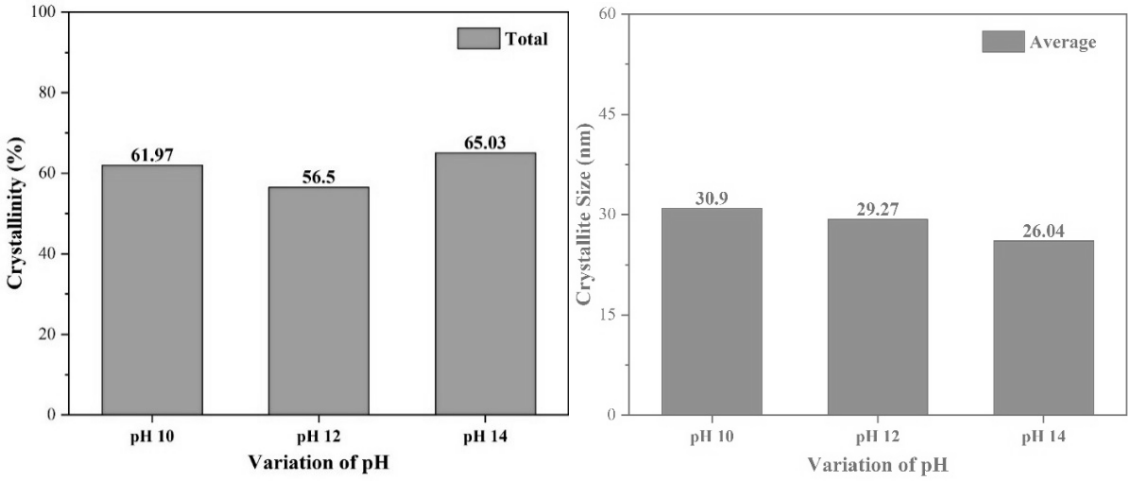

(a) (b)

Fig. 3. (a) Crystallinity, and (b) crystal size of photocatalyst composites at various pH.

Surface Area Analysis (SAA). pH synthesis has affected the surface area of composite as shown in Figure 4. Figure 4a displayed a type IV adsorption isotherm typical of mesoporous materials (2–50 nm), with an H3 (slit-shaped pores or plate-like aggregates) or H4 (wedge-shaped pores) hysteresis loop associated with slit or wedge-shaped pores formed by particle irregularities, non-uniform pore structures, incomplete or asymmetric openings, non-linear channels, and broad pore size distribution. Figure 4b showed that increasing the synthesis pH leads to a larger surface area. Under more alkaline conditions, greater lattice distortion and deformation of TiO_2 occur, allowing more Fe ions to incorporate and become trapped within the TiO_2 structure during restructuring, sintering, and condensation processes. From pH 10 to 12, the surface area increases along with larger pore volume and size, suggesting that the enhancement is attributed to the opening and expansion of internal pores resulting from higher doping levels and oxygen vacancies. The increased doping promotes greater lattice distortion, strain, bond breakage, oxygen defects, and changes in crystallinity. This effect was further supported by the blue shift of Raman spectra (Figure 1).

As the pH increased from 12 to 14, the pore volume and size decreased while the surface area increased, suggesting pore closure and the formation of new iron oxide pores. This change is attributed to the rapid precipitation of iron ions and hematite formation at pH = 14, which partially covers TiO_2 pores and enhances interfacial interactions leading to heterojunction formation, as evidenced by the red shift in the Raman spectra (Figure 1).

Bandgap analysis. The change in pH causes a variation in the interaction and distortion strength of the TiO_2 crystal and alters the formation of iron oxide, thereby affecting the doping strength and interfacial interactions. Then, in turn, the pH will influence the bandgap of the photocatalyst composite, as shown in Figure 5.

Figure 5 showed that TiO_2 has a bandgap of 3.21 eV, similar to other studies [29] and the composites bandgap decreases with increasing pH. This reduction is attributed to enhanced TiO_2 lattice distortion and deformation, which facilitate the incorporation and trapping of Fe ions as dopants during restructuring, sintering, and condensation. In addition, the higher the pH, the greater the formation of iron oxides, especially hematite, resulting in greater interfacial interactions and heterojunctions. The decrease in the bandgap due to increased doping is supported by a shift in the Raman spectra (Figure 1). Based on Figure 1 and Figure 5, it shows that the decrease in pH is due to the presence of iron ion doping and an increase in heterojunctions with increasing pH.

The TiO_2/Fe_2O_3 heterojunction forms through the coupling of two semiconductors with different band gaps. Due to TiO_2's higher Fermi energy and lower work function, electrons transfer from TiO_2 to Fe_2O_3 to equilibrate the Fermi levels [30]. Although this interaction does not directly alter intrinsic bandgap of TiO_2, the heterojunction enhances visible-light utilization, thereby improving photocatalytic performance [31].

Besides heterojunction formation, Fe^{3+} ion doping more contributes to bandgap narrowing. The substitution of Ti^{4+} by Fe^{3+} in the TiO_2 lattice introduces new energy states below the conduction band, reducing the overall bandgap energy [32,33]. The overlap between Ti 3d and Fe 3d orbitals increases with doping, enhancing electronic interaction and further narrowing the intrinsic bandgap of TiO_2 [9].

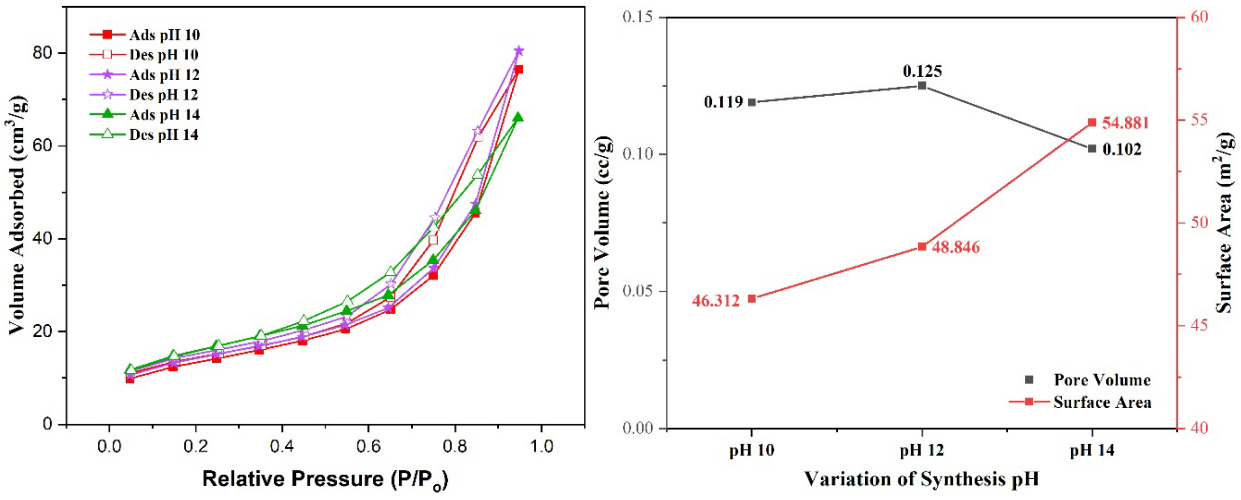

(a) (b)

Fig. 4. (a) Hysteresis loop isotherm, (b) Pore volume and surface area of composite with variation pH synthesis.

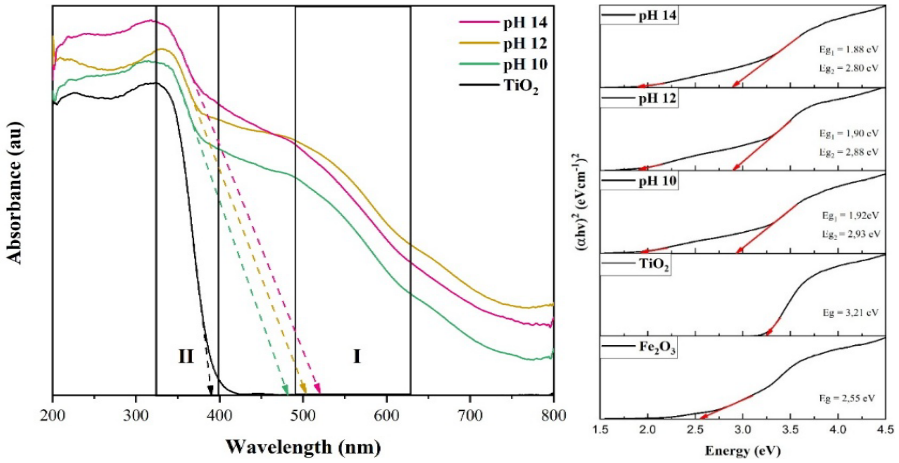

(a) (b)

Fig. 5. (a) DRS spectra, and (b) bandgap of the composite with variation pH synthesis.

VSM Analysis. Vibrating Sample Magnetometry (VSM) analysis was performed to investigate the alteration of magnetic properties in TiO_2 powders upon the simultaneous incorporation of Fe^{2+} and Fe^{3+} ions at pH variation, as shown in Figure 6. Figure 6 indicated that the composite exhibits soft magnetic behavior, characterized by a narrow hysteresis loop, low remanence (Mr), and low coercivity (Hc). Increasing pH decreases the saturation magnetization (Ms) due to the higher fraction of hematite (α-Fe_2O_3), which is antiferromagnetic, consistent with XRD results (Figure 2).

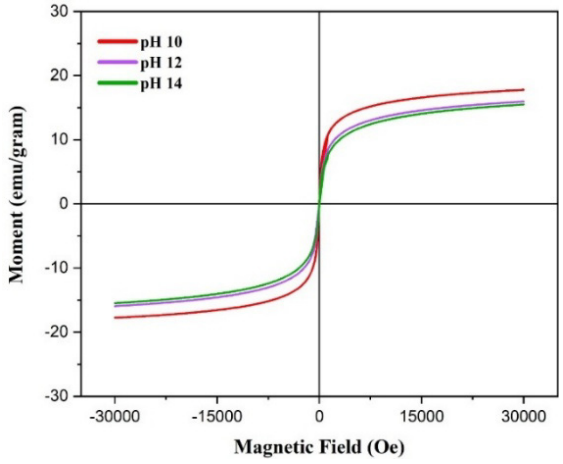

Fig. 6. Hysteresis Loop VSM composite with pH variation.

In hematite structure, Fe^{3+} ions occupy symmetrical octahedral sites with antiparallel spins, resulting in a nearly zero net magnetic moment. In contrast, maghemite contains Fe^{3+} ions in both octahedral and tetrahedral sites, creating cation imbalance and vacancies, which prevent complete spin cancellation, producing a measurable net magnetic moment [34-36]. Consequently, increasing Fe^{3+} shifted the composite from ferrimagnetic (maghemite-rich) toward antiferromagnetic (hematite-rich) behavior.

XPS Analysis. XPS spectra of TiO_2 and composites with pH variation as seen in Figure 7. The composite used in this study was the $TF_{0.1}$; $TF_{0.2}$; TF_1 composite with the composition of Fe^{2+}:Fe^{3+} = 1:2 (mole/mole), T = 90 °C, and pH = 12. Figure 7a showed the Fe 2p spectra of iron oxides, with two main peaks at 709.87 eV and 723.55 eV ($TF_{0.2}$), corresponding to Fe $2p_{3/2}$ and Fe $2p_{1/2}$ binding energies, respectively. The spin–orbit splitting energy (ΔBE) of 13.19 eV (>13.0 eV) confirms the presence of Fe^{3+} species (Madima et al., 2022; Mei et al., 2019; Yamashita et al., 2008; Yin et al., 2023). Figure 7b showed Ti 2p peaks at 456.76 eV ($2p_{3/2}$) and 462.38 eV ($2p_{1/2}$), with a spin splitting of 5.65–5.88 eV, confirming Ti^{4+}. At low Fe_2O_3 content (<$TF_{0.1}$), Ti 2p peaks shift positively, indicating interfacial interaction (heterojunction) and binary oxide formation [37], [38]. In contrast, at higher Fe_2O_3 loading ($TF_{0.2}$ and $TF_{1.0}$), binding energy of Ti 2p peaks shift negatively (~0.1–0.5 eV), signifying substitutional doping, where Fe^{3+} replaces Ti^{4+}, inducing charge imbalance, oxygen vacancies, and partial Ti^{4+} reduction to Ti^{3+}. A negative Ti 2p shift occurs (~0.1–0.5 eV) due to substitutional doping of Ti^{4+} by Fe^{3+}, which increases electron density, generates oxygen vacancies, and promotes Ti^{3+} formation as a charge compensation mechanism [39], [40]. The substitution of Fe^{3+} for Ti^{4+} generates a charge imbalance that induces oxygen vacancies and partial reduction of Ti^{4+} to Ti^{3+} for charge compensation. These oxygen defects create a more reducing environment, allowing Ti^{4+} to be reduced to Ti^{3+}, increasing electron density and weakening the nuclear binding energy, which leads to a negative shift in the Ti 2p binding energy. Consistently, binding energy of O 1s spectra (Figure 7c) also exhibits positive shifts (528.04 → 529.15 eV) with increasing Fe^{3+}, attributed to charge redistribution from Ti^{4+} substitution by Fe^{3+}, consistent with lattice distortion and oxygen vacancy formation [38], [39]. Based on Figure 7d-7f, the deconvoluted O 1s spectra showed a new peak at 531.17 eV, absent in pure TiO_2 (Figure 7d), which indicated the presence of oxygen vacancies, with intensity increasing

as Fe^{3+} content rises. The results demonstrated that higher Fe^{3+} content enhances oxygen vacancy formation and Fe–O–Ti bonding, mainly through substitutional doping [40]. Incorporation of Fe ions causes binding energy shifts in both Ti 2p peaks, indicating Fe–O–Ti bond formation.

3.1.2. Influence of Temperature

In this section, TiO_2-Fe/Fe_2O_3 photocatalyst have been synthezised with a constant mole ratio of TiO_2:Fe_2O_3 = 1:1/5 ($TF_{0.2}$). Meanwhile, the variation of temperature was carried out at 90 ºC (<boiling point) and 110 ºC (>boiling point). Based on the research, temperature has affected properties and photocatalytic activities of the photocatalyst.

Raman Analysis. The concentration of Fe^{2+} and Fe^{3+}, as well as the composition of Fe_2O_3 to TiO_2 powder influences Raman inelastic scattering, as shown in Figure 8. Figure 8 indicated that as temperature increased, peak shift towards lower wavenumbers (red shift) occurred, particularly the primary peak (E_{1g}) from 139.79 cm^{-1} to 135.65 cm^{-1}. Red shift (bathochromic) has shown an increase in interfacial and heterojunction interactions with increasing temperature. This is due to a significant increase in the formation and precipitation of $Fe(OH)_2$ and $Fe(OH)_3$ on the surface of TiO_2 powder as the temperature increases from 90 to 110 ºC. Below the boiling point (90 °C), the Raman spectrum of composite showed no Fe_2O_3 peaks, indicating that Fe dopants were successfully incorporated into the TiO_2 lattice by substituting Ti^{4+} sites [24]. Meanwhile, at higher temperatures above the boiling point (110 °C), the Raman spectrum shows a peak from Fe_2O_3 at 219.88 cm^{-1} and 286.07 cm^{-1}. It indicated the presence of iron oxide deposition on the TiO_2 surface forming interfacial and heterojunction interactions.

XRD Analysis. Temperature synthesis has affected the diffractogram pattern and crystallite composition of composite as shown in Figure 9. Figure 9a showed different diffractogram patterns between 90 and 110 ºC, showing different compositions of iron oxide formed at 90 and 110 ºC. At T = 90 ºC, the formation of maghemite (γ-Fe_2O_3) was dominant with the highest intensity at 2θ = 35,71º (311), while at T = 110 ºC, the formation of hematite (α-Fe_2O_3) was dominant as seen from the highest intensity at 2θ = 33.14º (104) as the main peak of hematite (α-Fe_2O_3). It showed that the higher temperature caused the transformation of maghemite (γ-Fe_2O_3) into hematite (α-Fe_2O_3) [11], [41]. It was supported by refinement analysis using HighScore Plus as seen in Figure 9b. At high temperature (110 °C), leading to oxidation of Fe^{2+} to be Fe^{3+} and then $Fe(OH)_3$ formation became higher. Consequently, calcination predominantly converts $Fe(OH)_3$ into hematite, resulting in higher hematite content at higher temperatures.

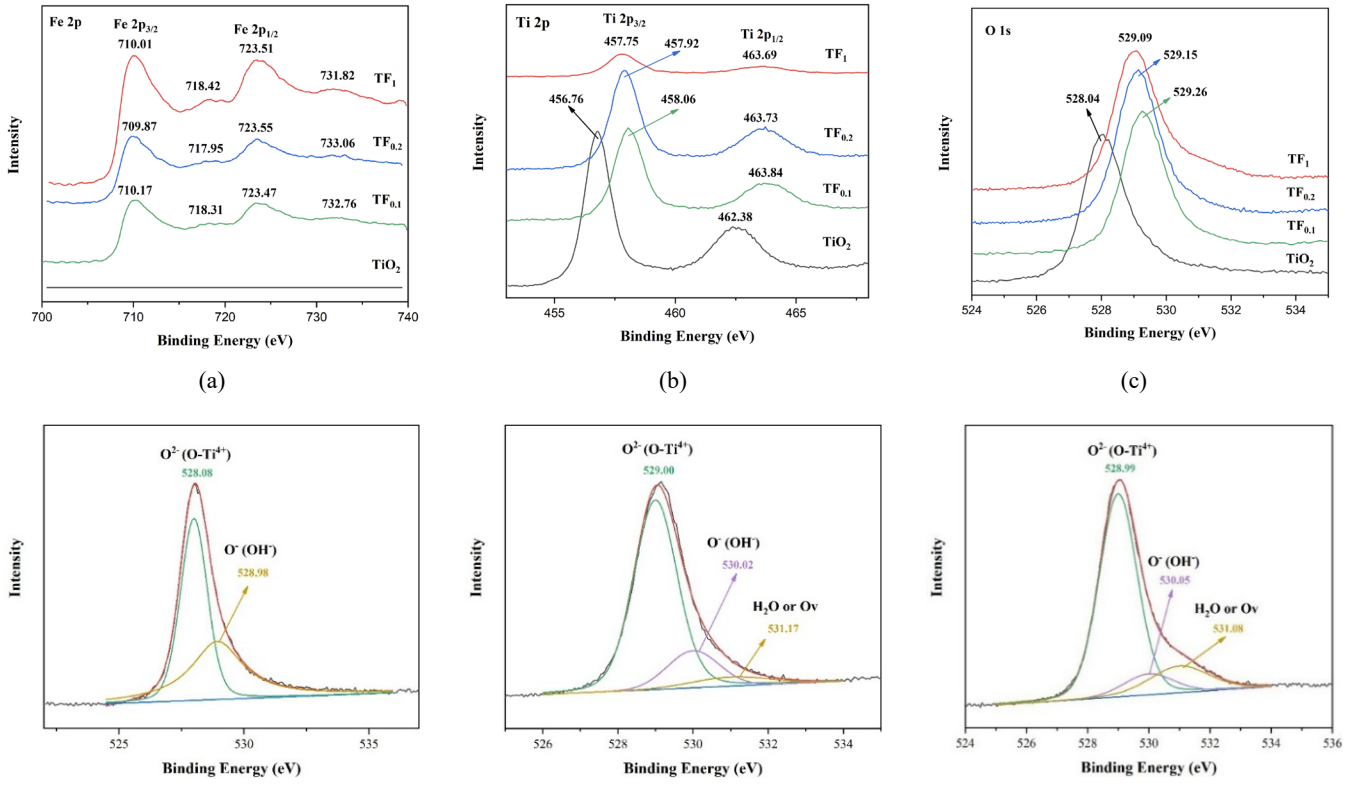

Fig. 7. XPS Spectra (a) high resolution spectra (HRS) of Ti2p peak, (b) deconvolution spectra Ti2p of $TF_{0.2}$, (c) deconvolution spectra Ti2p of TF_1, (d) deconvolution spectra O1s of TiO_2, (e) deconvolution spectra O1s of $TF_{0.2}$, (f) deconvolution spectra O1s of TF_1.

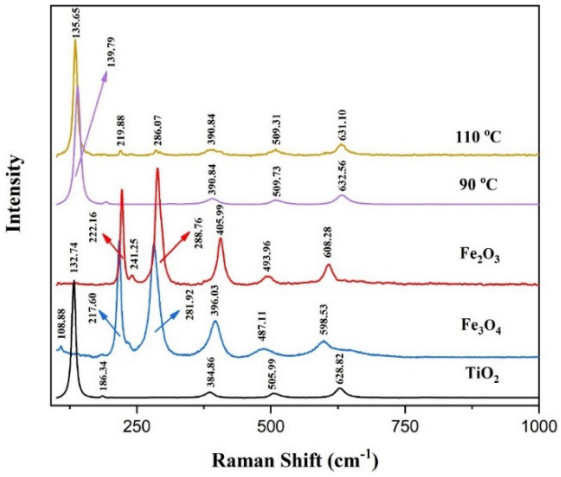

Fig. 8. Raman spectra of composites with variations in temperature synthesis.

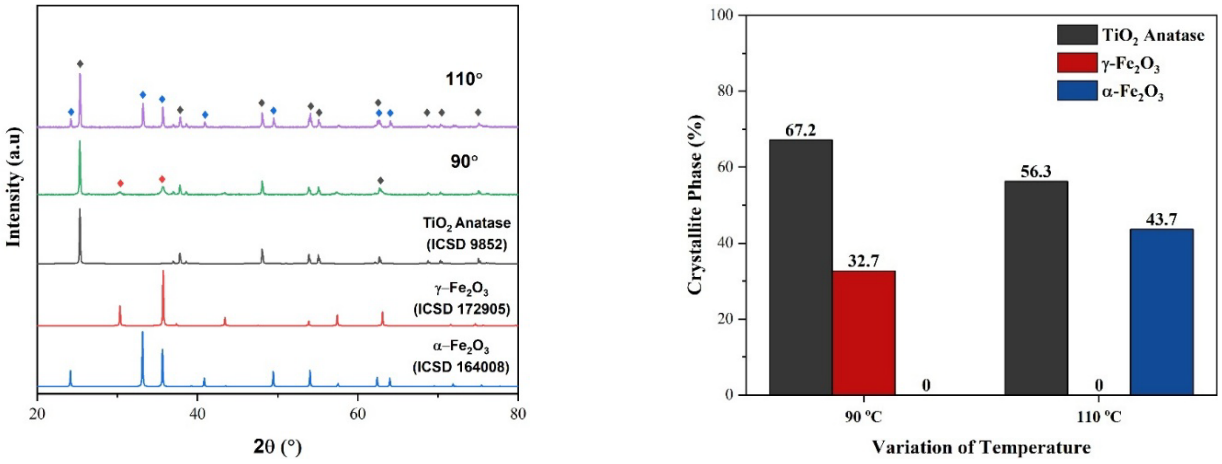

(a) (b)

Fig. 9. (a) XRD diffractogram, and (b) crystallite composition (%) of composite with temperature variation.

Alteration of temperature reaction also affected crystallinity and crystallite size, as seen in Figure 10. Figure 10a and 10b showed that increasing the reaction temperature enhances the crystallinity and crystal size of the photocatalyst composite.

As seen in Figure 9b, this increase in crystallinity is mainly attributed to the greater formation of hematite crystals with rising temperature, despite the decrease in TiO_2 crystal composition. At higher temperatures (110 °C), Fe^{2+} oxidation to Fe^{3+} and $Fe(OH)_3$ formation become more significant, leading to its transformation into hematite during calcination and resulting in higher hematite content.

The simultaneous increase in crystal size and decrease in TiO_2 crystallinity suggests molecular interfacial interaction (aggregation, sintering, agglomeration) between Fe_2O_3 and TiO_2. Elevated temperatures promote nucleation and condensation reactions between these molecules, contributing to crystal growth. Karami (2010) [41] also reported that heating facilitates the transformation of maghemite (γ-Fe_2O_3) to hematite (α-Fe_2O_3) and increases crystal size.

Surface Area Analysis (SAA). Alteration temperature has also affected the surface area of composite as shown in Figure 11. Figure 11 showed that increasing the temperature leads to a lower surface area. This is because of a significant increase in the formation and precipitation of $Fe(OH)_3$, leading to its transformation into hematite on the surface of TiO_2 powder and a decrease in the surface area of the composite as the temperature increases from 90 to 110 °C. The presence of iron oxide deposition on the TiO_2 surface forming interfacial and heterojunction interactions, then increased the crystallite size of the composite, as shown by the shift in the Raman spectra (Figure 8) and Figure 10. The interaction caused a covering of pores and decreased pore volume, as seen in Figure 11.

Bandgap analysis. The change in temperatures synthesis causes a variation in the interaction and distortion strength of the TiO_2 powder and alters the formation of iron oxide, thereby affecting the doping strength and interfacial interactions. Then, in turn, the temperatures will influence the bandgap of the photocatalyst composite, as shown in Figure 12.

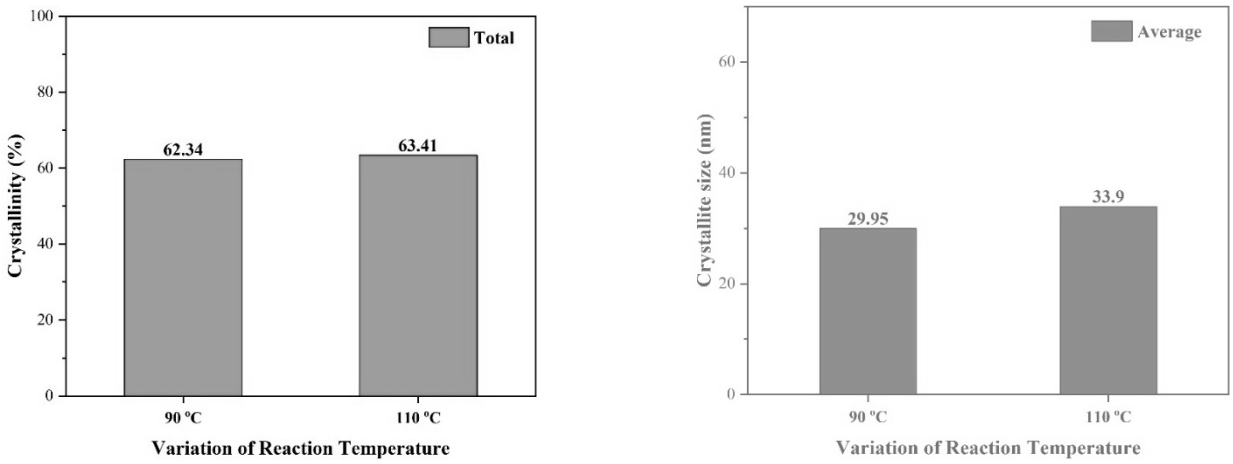

(a) (b)

Fig. 10. (a) Crystallinity, and (b) crystal size of composites at various temperature.

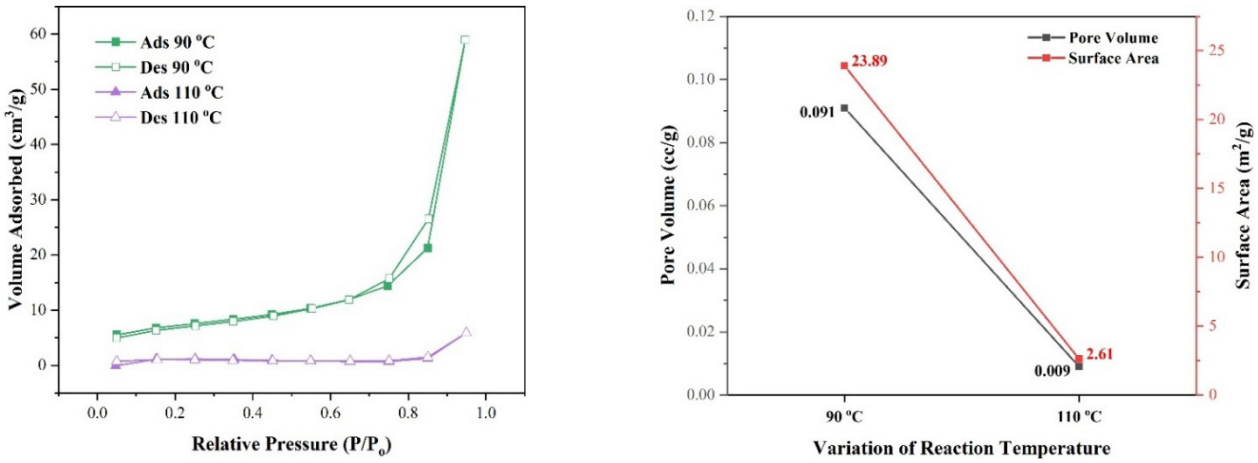

(a) (b)

Fig. 11. (a) Hysteresis loop isotherm, (b) Pore volume and surface area of composite with different temperature.

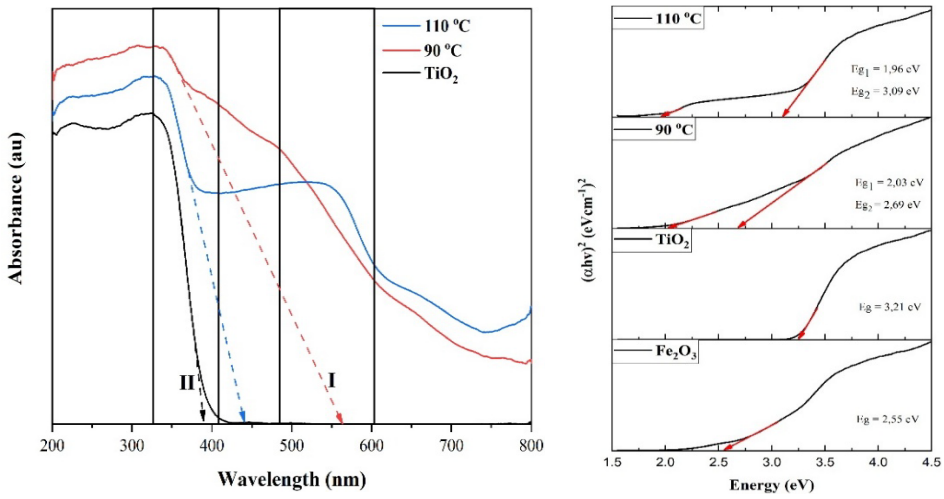

(a) (b)

Fig. 12. DRS spectra, and (b) bandgap of the composite with different temperature synthesis

Figure 12 showed that the bandgap increases with increasing temperature of reaction.

At elevated temperatures, the accelerated and increased formation of $Fe(OH)_2$ and $Fe(OH)_3$ substantially reduces lattice distortion induced by Fe^{2+}, Fe^{3+}, and OH^- ions.

As a result, structural disruption of TiO_2 is significantly minimized, leading to a markedly lower probability of Fe-ion incorporation into the lattice, while interfacial interactions and heterojunction formation become more dominant.

Consequently, the bandgap narrowing is more pronounced at lower temperatures. The TiO_2/Fe_2O_3 heterojunction is created through the coupling of two semiconductors with different band gaps.

Due to TiO_2's higher Fermi energy and lower work function, electrons transfer from TiO_2 to Fe_2O_3 to equilibrate the Fermi levels [30].

Although this interaction does not directly alter intrinsic bandgap of TiO_2, the heterojunction enhances visible-light utilization, thereby improving photocatalytic performance [31].

VSM Analysis. Vibrating Sample Magnetometry (VSM) analysis was performed to investigate the alteration of magnetic properties in TiO_2 powders with different temperature, as shown in Figure 13.

Figure 13 showed that simultaneous incorporation of Fe^{2+} and Fe^{3+} ions with higher temperature decreases the saturation magnetization (Ms) due to the dominant fraction of hematite (α-Fe_2O_3), which is antiferromagnetic, consistent with XRD results (Figure 9). Saturation magnetization (Ms) at 90 °C is 25,13 emu/gram, while at 110 °C is 0,77 emu/gram. At higher temperatures (110 °C), oxidation of Fe^{2+} to Fe^{3+} and then $Fe(OH)_3$ formation became higher.

Consequently, calcination predominantly converts $Fe(OH)_3$ into hematite and significantly decreased magnetic properties.

3.2. Application of the Composite for Cr (VI) Photoreduction and MV Photodegradation

3.2.1. Influence of pH

The variation in pH has affected photocatalysis activities. as shown in Figure 14. Figure 14 showed that the increasing pH enhances the photocatalytic activity of the composites under visible-light irradiation.

The improvement is attributed to narrowing bandgap, reduced crystallinity, increased surface area induced by heterojunction and ion Fe incorporation.

The higher the pH, the smaller the band gap and crystal size, while the surface area is larger. The Fe^{3+} ions can be incorporated and doped into the TiO_2 crystal, where Fe^{3+} ions can act as electron and hole traps [42-46].

Based on the results, MV degradation is more pronounced than Cr (VI) photoreduction, suggesting that Fe^{3+} primarily functions as an electron trap rather than a hole trap.

3.3. Influence of Temperature

The variation in temperature synthesis has affected photocatalysis activities. as shown in Figure 15.

Figure 15 showed that increasing pH decreases the photocatalytic activity of the composites under visible-light irradiation because of increasing bandgap, crystal size, and crystallinity and decreasing surface area, as shown in Figure 10–12.

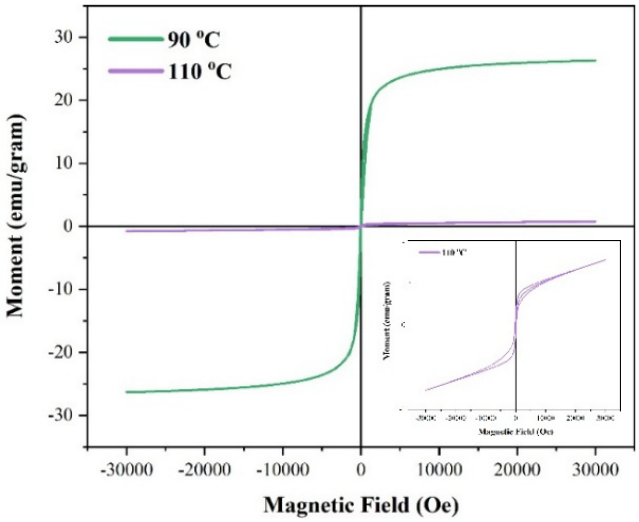

Fig. 13. Hysteresis Loop VSM composite with different temperature synthesis (insert: Hysteresis Loop at 110 °C).

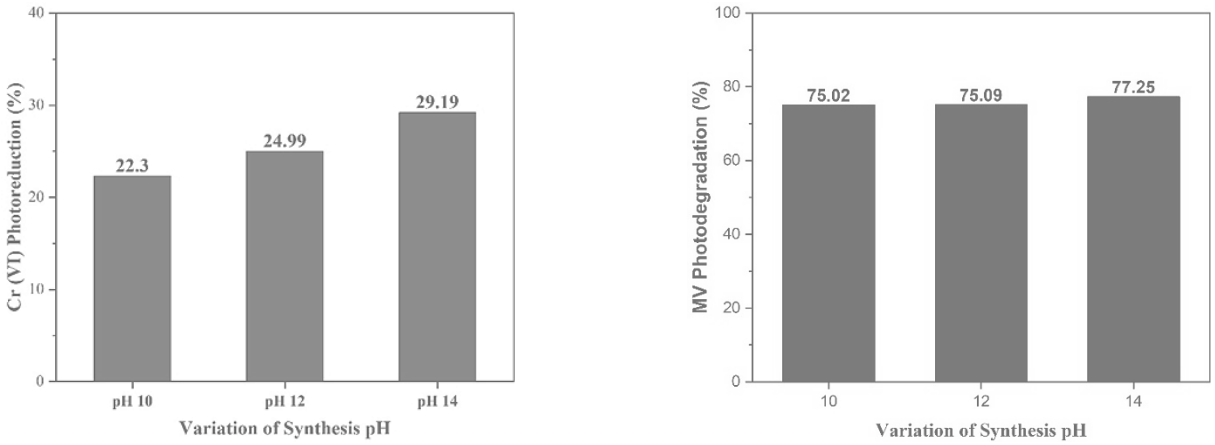

(a) (b)

Fig. 14. (a) photoreduction of Cr(VI) (b) MV photodegradation with different pH.

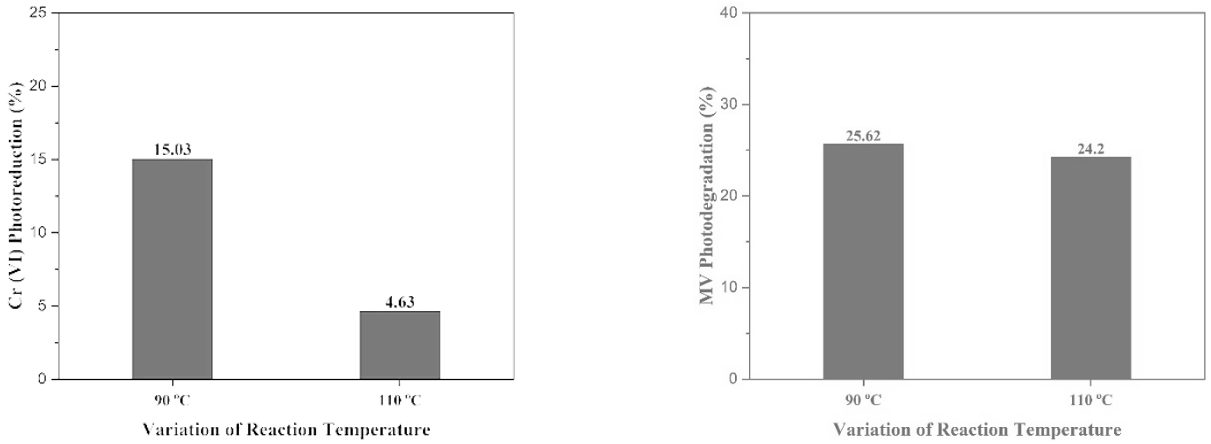

(a) (b)

Fig. 15. (a) photoreduction of Cr(VI) (b) MV photodegradation with different temperature.

4. Conclusion

Modification of TiO_2 powder by simultaneous addition of Fe^{2+} and Fe^{3+} ions with different pH and temperature synthesis has affected the structural, optical, electronic, magnetic, and photocatalytic activity of TiO_2 powder.

The higher the pH of the synthesis has caused a decrease in magnetic properties, TiO_2 crystal composition, crystal size, and band gap, but increase surface area, thus causing an increase in photocatalytic activity under visible light radiation.

The higher temperature synthesis (110 °C) has caused a decrease in magnetic properties, TiO_2 crystal composition, surface area, but increase crystal size, crystallinity, and band gap, thus causing a decrease in photocatalytic activity under visible light radiation.

Acknowledgements

This work was supported by the Doctoral Dissertation Research Grant (PDD) 2024 from Universitas Sebelas Maret (UNS) and the Ministry of Higher Education, Science, and Technology, Republic of Indonesia with grant numbers 194.2/UN27.22/PT.01.03/2024.

References

[1] Kubiak, M. Kubacka, E. Gabała, A. Dobrowolska, K. Synoradzki, K. Siwińska-Ciesielczyk, K. Czaczyk, and T. Jesionowski. Hydrothermally assisted fabrication of TiO_2-Fe_3O_4 composite materials and their antibacterial activity. *Materials*, 13(21) (2020), pp. 1–23. doi: https://doi.org/10.3390/ma13214715.

[2] D. Beketova, M. Motola, H. Sopha, J. Michalicka, V. Cicmancova, F. Dvorak, L. Hromadka, B. Frumarova, M. Stoica, J.M. Macak. One-Step Decoration of TiO2 Nanotubes with Fe3O4 Nanoparticles: Synthesis and Photocatalytic and Magnetic Properties. *ACS Appl Nano Mater*, 3(2) (2020), pp. 1553–1563. doi: https://dx.doi.org/10.1021/acsanm.9b02337 .

[3] I. M. Ramírez-Sánchez and E. R. Bandala. Photocatalytic degradation of estriol using iron-doped TiO2 under high and low UV irradiation. *Catalysts*, 8(12) (2018). doi: 10.3390/catal8120625.

[4] M. Stefan, O. Pana, C. Bele, D. Sillipas, M. Senila, E. Gautron. Synthesis and characterization of Fe_3O_4-TiO_2 core shell nanoparticles. J. Appl. Phys. 116 (2014). http://dx.doi.org/10.1063/1.4896070.

[5] M. Safari, R. Talebi, M. H. Rostami, M. Nikazar, and M. Dadvar. Synthesis of iron-doped TiO_2 for degradation of reactive Orange16. *J Environ Health Sci Eng* 12(1) (2014), pp. 1–8. doi: http://www.ijehse.com/content/12/1/19.

[6] D. Liang, S. Liu, Z. Wang, Y. Guo, W. Jiang, C. Liu, H. Wang, N. Wang, W. Ding, L. Wang, S. Xu. Coprecipitation synthesis of N, Fe doped anatase TiO_2 nanoparticles and photocatalytic mechanism. *Journal of Materials Science: Materials in Electronics*, 30(13) (2019), pp. 12619–12629, doi: https://doi.org/10.1007/s10854-019-01623-3.

[7] G. Cheng, X. Liu, X. Song, X. Chen, W. Dai, R. Yuan, X. Fu. Visible-light-driven deep oxidation of NO over Fe doped TiO_2 catalyst: Synergic effect of Fe and oxygen vacancies. *Appl Catal B*, 277(2020), doi: https://doi.org/10.1016/j.apcatb.2020.119196.

[8] V. Moradi, M. B. G. Jun, A. Blackburn, and R. A. Herring. Significant improvement in visible light photocatalytic activity of Fe doped TiO_2 using an acid treatment process. *Appl Surf Sci*, 427 (2018), pp. 791–799, doi: http://dx.doi.org/10.1016/j.apsusc.2017.09.017.

[9] N. Rathore, R. K. Shukla, K. C. Dubey, and A. Kulshreshtha. Synthesis of undoped and Fe doped nanoparticles of TiO_2 via co-precipitation technique and their characterizations. *Mater Today Proc*, 29(2020), pp. 861–865, doi: https://doi.org/10.1016/j.matpr.2020.05.072.

[10] N. Madima, K. K. Kefeni, S. B. Mishra, A. K. Mishra, and A. T. Kuvarega. Fabrication of magnetic recoverable Fe_3O_4/TiO_2 heterostructure for photocatalytic degradation of Rhodamine B dye. *Inorg Chem Commun,* 145 (2022), pp. 1–13, doi: https://doi.org/10.1016/j.inoche.2022.109966.

[11] A. Bouziani, J. Park, and A. Ozturk. Synthesis of α-Fe_2O3/TiO_2 heterogeneous composites by the sol-gel process and their photocatalytic activity. *J Photochem Photobiol A Chem*, 400 (2020), p. 112718, doi: https://doi.org/10.1016/j.jphotochem.2020.112718.

[12] R. Hatefi, H. Younesi, A. Mashinchian-Moradi, and S. Nojavan. A facile decoration of anatase Fe_3O_4/TiO_2 nanocomposite with graphene quantum dots: Synthesis, characterization, and photocatalytic activity. *Advanced Powder Technology*, 32(7) (2021), pp. 2410–2422, doi: https://doi.org/10.1016/j.apt.2021.05.020.

[13] F. Parast, M. Montazeri-Pour, M. Rajabi, and F. Bavarsiha. Comparison of the structural and photo-catalytic properties of nanostructured Fe_3O_4/TiO_2 core-shell composites synthesized by ultrasonic and stöber methods. *Science of Sintering,* 52(4) (2020), pp. 415–432, doi: https://doi.org/10.2298/SOS2004415P.

[14] C. N. C. Hitam and A. A. Jalil. A review on exploration of Fe_2O_3 photocatalyst towards degradation of dyes and organic contaminants. *J Environ Manage*, 258 (2020), p. 110050, doi: https://doi.org/10.1016/j.jenvman.2019.110050.

[15] E. Xie, L. Zheng, Y. Wang, J. Dou, A. Ding, D. Zhang. One-step synthesis of magnetic-TiO_2-nanocomposites with high iron oxide-composing ratio for photocatalysis of rhodamine 6G. *PLoS One*, 14 (8) (2019), pp. 1–19, doi: https://doi.org/10.1371/journal.pone.0221221.

[16] O. Monfort and G. Plesch. Bismuth vanadate-based semiconductor photocatalysts: a short critical review on the efficiency and the mechanism of photodegradation of organic pollutants. *Environmental Science and Pollution Research*, 25(20) (2028), pp. 19362–19379, doi: 10.1007/s11356-018-2437-9.

[17] V. V. Shymanovska, T. A. Khalyavka, E. V. Manuilov, T. A. Gavrilko, A. Aho, V. V. Naumov, and N. D. Shcherban. Effect of surface doping of TiO_2 powders with Fe ions on the structural, optical and photocatalytic properties of anatase and rutile. *Journal of Physics and Chemistry of Solids*, 160(2022), p. 110308. doi: https://doi.org/10.1016/j.jpcs.2021.110308.

[18] C. Afonso, O. Lima, I.R. Segundo, S. Landi, E. Margalho, N. Homem, M. Pereira, M.F.M. Costa, E. Freitas, and J. Carneiro. Effect of Iron-Doping on the structure and photocatalytic activity of TiO_2 nanoparticles. *Catalysts,* 13(1) (2023), doi: https://doi.org/10.3390/catal13010058.

[19] A. H. A. Gonçalves, P. H. C. Siciliano, O. C. Alves, D. V. Cesar, C. A. Henriques, and A. B. Gaspar. Synthesis of a Magnetic Fe_3O_4/RGO Composite for the Rapid Photo-Fenton Discoloration of Indigo Carmine Dye. *Top Catal*, 63(11) (2020), pp. 1017–1029, doi: https://doi.org/10.1007/s11244-020-01277-0.

[20] C. Van Tran, P. T. H. Nguyen, D. D. Nguyen, H. T. T. Pham, D. T. Do, and D. D. La. Facile Fabrication of Fe_2O_3/TiO_2 Composite from Titanium Slag as Adsorbent for As(V) Removal from Aqueous Media. *Sustainability (Switzerland)*, 15(9) (2023), doi: https://doi.org/10.3390/su15097253.

[21] T. T. Loan, V. H. Huong, N. T. Huyen, L. Van Quyet, N. A. Bang, and N. N. Long. Anatase to rutile phase transformation of iron-doped titanium dioxide nanoparticles: The role of iron content. *Opt Mater (Amst)*, 111(2021), doi: https://doi.org/10.1016/j.optmat.2020.110651.

[22] A. P. Singh, R. B. Wang, C. Tossi, I. Tittonen, B. Wickman, and A. Hellman. Hydrogen induced interface engineering in Fe_2O_3-TiO_2 heterostructures for efficient charge separation for solar-driven water oxidation in photoelectrochemical cells. *RSC Adv*, 11(8) (2021), pp. 4297–4307, doi: https://doi.org/10.1039/d0ra09655e.

[23] P. Sun, S. Han, J. Liu, J. Zhang, S. Yang, F. Wang, W. Liu, S. Yin, Z. Ning, W. Cao. Introducing oxygen vacancies in TiO_2 lattice through trivalent iron to enhance the photocatalytic removal of indoor NO. *International Journal of Minerals, Metallurgy and Materials*, 30(10) (2023), pp. 2025–2035, doi: https://doi.org/10.1007/s12613-023-2611-z.

[24] R. A. Solano, A. P. Herrera, D. Maestre, and A. Cremades. Fe-TiO_2 Nanoparticles Synthesized by Green Chemistry for Potential Application in Waste Water Photocatalytic Treatment. *J Nanotechnol*, 2019 (2019), doi: https://doi.org/10.1155/2019/4571848.

[25] H. Jiang, F. Zhao, and S. Zang. Magnetically recoverable B,F,P-TiO_2/Fe_3O_4 nanophotocatalyst with enhanced charge separation efficiency. *Mater Sci Semicond Process*, 75 (2018), pp. 103–111, doi: https://doi.org/10.1016/j.mssp.2017.11.012.

[26] P. S. Pinto, G. D. Lanza, J. D. Ardisson, and R. M. Lago. Controlled dehydration of $Fe(OH)_3$ to Fe_2O_3: Developing mesopores with complexing iron species for the adsorption of β-lactam antibiotics. *J Braz Chem Soc*, 30(2) (2018), pp. 310–317, doi: http://dx.doi.org/10.21577/0103-5053.20180179.

[27] M. S. Khan, J. A. Shah, N. Riaz, T. A. Butt, A. J. Khan, W. Khalifa, H. H. Gasmi, E. R. Latifee, M. Arshad, A.A.A. Al-Naghi, A. Ul-Hamid, M. Arshad, M. Bilal. Synthesis and characterization of Fe-TiO_2 nanomaterial: Performance evaluation for rb5 decolorization and in vitro antibacterial studies. *Nanomaterials*, 11 (2021), doi: https://doi.org/10.3390/nano11020436.

[28] J. A. A. Abdullah, Á. Díaz-García, J. Y. Law, A. Romero, V. Franco, and A. Guerrero. Quantifying the Structure and Properties of Nanomagnetic Iron Oxide Particles for Enhanced Functionality through Chemical Synthesis. *Nanomaterials*, 13(15) (2023), doi: https://doi.org/10.3390/nano13152242.

[29] M. Praveendaniel and P. Rajesh Anantha Selvan. Synthesis and Application of TiO_2-Phosphomolybdic acid nanocomposite. *Journal of Chemistry Letters*, vol. 4(2) (2023), pp. 117–129, doi: https://doi.org/10.22034/JCHEMLETT.2023.395693.1114.

[30] Q. Mei, F. Zhang, N. Wang, Y. Yang, R. Wu, and W. Wang. TiO_2/Fe_2O_3 heterostructures with enhanced photocatalytic reduction of Cr(vi) under visible light irradiation. *RSC Adv*, 9(39) (2019), pp. 22764–22771, doi: https://doi.org/10.1039/c9ra03531a.

[31] Y. Q. Cao, T. Q. Zi, X. R. Zhao, C. Liu, Q. Ren, J. B. Fang, W. M. li, A. D. Li. Enhanced visible light photocatalytic activity of Fe_2O_3 modified TiO_2 prepared by atomic layer deposition. *Sci Rep*, 10(1) (2020), doi: https://doi.org/10.1038/s41598-020-70352-z.

[32] D. I. Anwar and D. Mulyadi. Synthesis of Fe-TiO_2 Composite as a Photocatalyst for Degradation of Methylene Blue. *Procedia Chem*, 17 (2015), pp. 49–54, doi: https://doi.org/10.1016/j.proche.2015.12.131.

[33] A. Khalid, P. Ahmad, A.I. Alharth, S. Muhammad, M.U. Khandaker, M.R.I. Faruque, I.U. Din, and M.A. Alotaibi. A practical method for incorporation of Fe (III) in Titania matrix for photocatalytic applications," *Mater Res Express 2021*, 8(4), doi: https://doi.org/10.1088/2053-1591/abf2e9.

[34] M. Coduri, P. Masala, L. Bianco, F. Spizzo, D. Ceresoli, C. Castellano, S. Cappelli, C. Oliva, S. Checchia, M. Allieta, D.V. Szabo, S. Schlabach, M. Hagelstein, C. Ferrero, and M. Scavini. Local structure and magnetism of Fe_2O_3 maghemite nanocrystals: The role of crystal dimension. *Nanomaterials*, 10(5) (2020), doi: https://doi.org/10.3390/nano10050867.

[35] J. A. Cuenca, K. Bugler, S. Taylor, D. Morgan, P. Williams, J. Bauer, and A. Porch. Study of the magnetite to maghemite transition using microwave permittivity and permeability measurements. *Journal of Physics Condensed Matter*, 28(10) (2016), doi: https://doi.org/10.1088/0953-8984/28/10/106002.

[36] Ö. Özdemir, D. J. Dunlop, and B. M. Moskowitz. The effect of oxidation on the Verwey transition in magnetite. *Geophys Res Lett*, 20(16) (1993), pp. 1671–1674, doi: https://doi.org/10.1029/93GL01483.

[37] A. Srivastava, J.A.K. Satrughna, M.K. Tiwari, A. Kanwade, S.C. Yadav, K. Bala, and P.M. Shirage. Effect of $Ti_{1-x}Fe_xO_2$ photoanodes on the performance of dye-sensitized solar cells utilizing natural betalain pigments extracted from Beta vulgaris (BV). *Energy Advances*, 2(1)(2023), pp. 148–160, doi: https://doi.org/10.1039/d2ya00197g.

[38] N. Kanjana, W. Maiaugree, P. Poolcharuansin, and P. Laokul. Synthesis and characterization of Fe-doped TiO_2 hollow spheres for dye-sensitized solar cell applications. *Materials Science and Engineering: B*, 271(2021), doi: https://doi.org/10.1016/j.mseb.2021.115311.

[39] A. M. Oviedo, H. Truong Thi, Q. C. Van, and H. H. Nguyen. Physicochemical properties of Fe-doped TiO_2 and the application in Dye-sensitized solar cells. *Opt Mater (Amst)*, vol. 137, doi: https://doi.org/10.1016/j.optmat.2023.113587.

[40] C. Wen, X., Ni, M. Han, Y. Yu, C. Liu, Y. Zhang, B. Zheng, and S. Feng. The Function of Photocatalytic Performance and Carrier Separation Efficiency Tuned by Doping Content in Homogeneous Photocatalysts. *Advanced Science*, 12(25) (2025), doi: https://doi.org/10.1002/advs.202501026.

[41] H. Karami. Synthesis and characterization of iron oxide nanoparticles by solid state chemical reaction method. *J Clust Sci*, 21(2010), pp. 11–20, doi: https://doi.org/10.1007/s10876-009-0278-x.

[42] M. Ghorbanpour and A. Feizi. Iron-doped TiO_2 Catalysts with Photocatalytic Activity. *J. Water Environ. Nanotechnol*, 4(1) (2019), pp. 60–66, doi: https://doi.org/10.22090/jwent.2019.01.006.

[43] C. Liao, Y. Li, and S. C. Tjong. Visible-light active Titanium dioxide nanomaterials with bactericidal properties. *Nanomaterials*, 10(124) (2020), doi: https://doi.org/10.3390/nano10010124.

[44] S. S. Bahri, Z. Harun, W. N. W. Saleh, R. Hussin, N. H. H. Hairom, N. H. Kamaruddin, H. Basri, N. I. Rasli, A. Rosman, M. R. Jamaluddin, and R. Ainuddin. Green synthesis and characterization of fe doped tio2 nanoparticles using lawsonia inermis leaf aqueous extracts as reductant for photocatalytic activity. *ASEAN Engineering Journal*, 13(3) (2023), pp. 141–152, doi: https://doi.org/10.11113/aej.V13.19690.

[45] T. Ali, P. Tripathi, A. Azam, W. Raza, A. S. Ahmed, A. Ahmed, and M. Muneer. Photocatalytic performance of Fe-doped TiO_2 nanoparticles under visible-light irradiation. *Mater Res Express*, 4(1) (2017), doi: https://doi.org/10.1088/2053-1591/aa576d.

[46] A. A. Isari, A. Payan, M. Fattahi, S. Jorfi, and B. Kakavandi. Photocatalytic degradation of rhodamine B and real textile wastewater using Fe-doped TiO_2 anchored on reduced graphene oxide (Fe-TiO_2/rGO): Characterization and feasibility, mechanism and pathway studies. *Appl Surf Sci*, 462(2018), pp. 549–564, doi: https://doi.org/10.1016/j.apsusc.2018.08.133